

## Substituent Effects

## Exquisite 1D Assemblies Arising from Rationally Designed Asymmetric Donor–Acceptor Architectures Exhibiting Aggregation-Induced Emission as a Function of Auxiliary Acceptor Strength

Roop Shikha Singh, Sujay Mukhopadhyay, Arnab Biswas, and Daya Shankar Pandey\*<sup>[a]</sup>

**Abstract:** One-dimensional nanostructures with aggregation-induced emission (AIE) properties have been fabricated to keep the pace with growing demand from optoelectronics applications. The compounds 2-[4-(4-methylpiperazin-1-yl)benzylidene]malononitrile (**PM1**), 2-[4-[4-(pyridin-2-yl)piperazin-1-yl]benzylidene]malononitrile (**PM2**), and 2-[4-[4-(pyrimidin-2-yl)piperazin-1-yl]benzylidene]malononitrile (**PM3**) have been designed and synthesized by melding piperazine and dicyanovinylene to investigate AIE in an asymmetric donor–acceptor (D–A) construct of A'–D– $\pi$ –A topology. The synthetic route has been simplified by using phenylpiperazine as a weak donor (D), dicyanovinylene as an acceptor (A), and pyridyl/pyrimidyl groups (**PM2/PM3**) as auxiliary acceptors (A'). It has been established that A' plays

a vital role in triggering AIE in these compounds because the same D–A construct led to aggregation-caused quenching upon replacing A' with an electron-donating ethyl group (**PM1**). Moreover, the effect of restricted intramolecular rotation and twisted intramolecular charge transfer on the mechanism of AIE has also been investigated. Furthermore, it has been clearly shown that the optical disparities of these A'–D– $\pi$ –A architectures are a direct consequence of comparative A' strength. Single-crystal X-ray analyses provided justification for role of intermolecular interactions in aggregate morphology. Electrochemical and theoretical studies affirmed the effect of the A' strength on the overall properties of the A'–D– $\pi$ –A system.

## Introduction

The fabrication of functional soft materials through controlled self-assembly of molecular building blocks has proven to be extremely valuable in the construction of various hierarchical assemblies.<sup>[1]</sup> Among these, 1D nanostructures have attracted particular attention owing to their significant role in the construction of high-performance optoelectronic devices, such as field-effect transistors (FETs), organic light-emitting diodes (OLEDs), organic light-emitting transistors (OLETs), and solar cells.<sup>[2]</sup> However, the realization of their full potential has been a daunting task due to the aggregation-caused quenching (ACQ) effect. After the discovery of aggregation-induced emission (AIE) by Tang and co-workers,<sup>[3]</sup> the area of AIE luminogens has expanded its horizon from blue- to red-emitting luminophores.<sup>[4,5]</sup> The mechanistic interpretation of AIE relies on several processes, including restricted intramolecular rotation (RIR), J-aggregate formation, excimer emission, and twisted intramolecular charge transfer (TICT).<sup>[6]</sup> With the addition of AIE, it has been possible to control aggregate buildup through the

strategic tuning of intermolecular interactions, leading to nanostructures of desired morphology and tunable solid-state emission. Through our earlier work, we have tried to devise a simplified approach toward optical and morphological control in AIE luminogens.<sup>[7]</sup> Following the same strategy, we intended to create 1D solid-state fluorescent nanostructures, in particular, twisted or helical nanofibers because they are endowed with distinct optical and photophysical properties that broaden their technological applications (see above).

The AIE luminogens developed so far are blue or green emitters. Red/yellow emitters are relatively scarce and generally endowed with appropriate  $\pi$ -conjugated donor (D) and acceptor (A) molecules, which lead to significantly redshifted emission through intramolecular charge transfer (ICT). In this context, numerous systems that exhibit fascinating optoelectronic properties have been successfully developed by various groups.<sup>[8]</sup> Furthermore, along with conventional symmetrical D–A systems, current research has also focused on asymmetric D–A molecules. The presence of more than one D/A unit with competitive strength unleashes interesting aspects of the push–pull mechanism, which may enable adjustments in the molecular structure and desired optoelectronic properties.<sup>[9]</sup> As an efficient A, dicyanovinylene (DCV) has found wide applications in the construction of symmetric and asymmetric D–A architectures with resourceful usage in organic photovoltaics (OPVs).<sup>[9b,10]</sup> Lately, some reports on AIE-active DCV derivatives

[a] R. S. Singh, S. Mukhopadhyay, A. Biswas, Prof. D. S. Pandey  
Department of Chemistry, Faculty of Science  
Banaras Hindu University, Varanasi 221 005 U.P. (India)  
E-mail: dspbhu@bhu.ac.in

Supporting information for this article is available on the WWW under <http://dx.doi.org/10.1002/chem.201503570>.

based on conventional tetraphenylethylene (TPE) donors, involving only modification in the strength of A, have surfaced.<sup>[11]</sup> None of these reports deal with nanostructures of desired morphology with AIE attributes.

Herein, we report on a system with asymmetric D–A architecture to control AIE as a function of A strength. Our prime concern was to set up a morphological trademark for achieving 1D nanostructures with AIE characteristics. Considering the applicability of flexible spacers in creating helical nanostructures, piperazine has been chosen to provide conformational flexibility in the scaffold.<sup>[12]</sup> Phenylpiperazine has been employed as D, whereas DCV has been used as the main A and pyridyl/pyrimidyl as auxiliary acceptors (A'). To ensure that AIE is unique to this A'–D– $\pi$ –A system and largely tuned through competition between the As, an ethyl group has been incorporated as an electron-donating substituent on the piperazine core to offer a symmetric D– $\pi$ –A construct. Herein, we present three strategically designed piperazine–DCV-based symmetric (2-[4-(4-methylpiperazin-1-yl)benzylidene]malononitrile (**PM1**)) and asymmetric (2-[4-[4-(pyridin-2-yl)piperazin-1-yl]benzylidene]malononitrile (**PM2**) and 2-[4-[4-(pyrimidin-2-yl)piperazin-1-yl]benzylidene]malononitrile (**PM3**)) D–A architectures, and a systematic study on the effect of substituents on their properties. Possessing a simple ethyl donor, symmetric **PM1** was AIE inactive, whereas the A' pyridyl and pyrimidyl moieties in **PM2** and **PM3** satisfied both steric and electronic requirements and bestowed them with AIE activity.

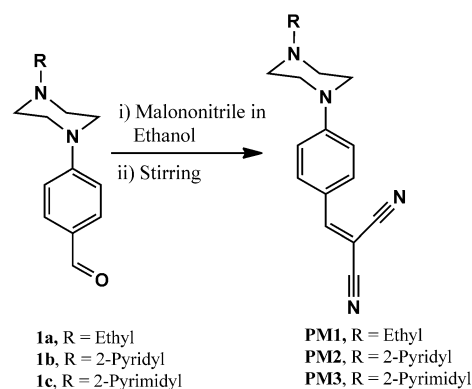
## Result and Discussion

### Synthesis and characterization of **PM1**–**PM3**

The aldehydes 4-(4-ethylpiperazin-1-yl)benzaldehyde (**1a**), 4-[4-(pyridin-2-yl)piperazin-1-yl]benzaldehyde (**1b**), and -[4-(pyrimidin-2-yl)piperazin-1-yl]benzaldehyde (**1c**) were synthesized by following procedures reported in the literature.<sup>[13]</sup> These aldehydes reacted with malononitrile in the presence of catalytic amounts of piperidine to afford **PM1**, **PM2**,<sup>[14]</sup> and **PM3** in reasonably good yield (70%, **PM1**; 88%, **PM2**; 90%, **PM3**). The syntheses of **PM1**–**PM3** are depicted in Scheme 1. All compounds were thoroughly characterized by elemental analyses, HRMS, and <sup>1</sup>H and <sup>13</sup>C NMR spectroscopy (Figures S1–S5 in the Supporting Information). The molecular structure of **PM3** was confirmed by X-ray single-crystal analysis. The compounds under investigation exhibited good solubility in THF, acetonitrile, DMF, DMSO, and dichloromethane; moderate solubility in methanol and ethyl acetate; and poor solubility in nonpolar solvents.

### Photophysical properties

The optical properties of **PM1**–**PM3** have been investigated by electronic absorption and emission spectral studies in THF ( $c = 5 \times 10^{-5} \text{ mol L}^{-1}$ ), and the resulting spectra are depicted in Figure S6 in the Supporting Information. In the absorption spectra, these compounds displayed absorption bands at  $\lambda = 425$ , 424, and 423 nm, respectively. The occurrence of absorption



Scheme 1. Synthetic route to **PM1**–**PM3**.

bands for **PM1**, **PM2** and **PM3** at almost the same position indicated comparable conjugation lengths in these molecules. Upon excitation at  $\lambda = 425$ , 424 and 423 nm, compounds **PM1**–**PM3** display weak locally excited (LE) emission bands at  $\lambda \approx 485$  nm with appreciable Stokes shifts (SSs; **PM1**:  $\lambda = 481$  nm, SS, 56 nm; **PM2**:  $\lambda = 488$  nm, SS, 64 nm; **PM3**:  $\lambda = 494$  nm, SS, 71 nm).

Possessing A'–D– $\pi$ –A architecture, these compounds are expected to show TICT behavior marked by charge separation between D and A units. In polar solvents, intramolecular rotation brings the luminogen from the LE to TICT state, featuring quenched and redshifted emission. This prompted us to investigate the photophysical behavior of **PM1**–**PM3** as a function of solvent polarity. Whereas there was no significant change in the absorption behavior of these molecules in different solvents, the fluorescence spectra were quite different, except for **PM1**. Both **PM2** and **PM3** displayed redshifted emissions in polar solvents (Figure 1). With changes in solvent polarity from extremely nonpolar to polar, redshifts of 20 and 40 nm were observed for **PM2** and **PM3**, respectively. It is worth mentioning that the emission intensity of **PM2** and **PM3** diminished in polar solvents (Figure S9 in the Supporting Information). To affirm this, we calculated the solvent polarity parameters ( $\Delta f$ ) for all solvents under investigation and tried to establish a relationship between emission intensity and  $\Delta f$  for **PM2** and **PM3** (Figure S9c in the Supporting Information). The plot of emission intensity versus  $\Delta f$  displayed a downward curve, which also supported the vulnerability of the excited state to decay through nonradiative processes in polar solvents, leading to emission quenching.<sup>[4b]</sup> It has been observed that the variation in emission intensity with solvent polarity was more consistent in **PM3** than **PM2**. These results suggested that **PM3** showed better solvatochromic behavior and enhanced ICT than **PM2**. Moreover, the excitation spectra of **PM2** and **PM3**, monitored at  $\lambda = 488$  and 494 nm (Figure 2), revealed that the absorption spectra did not match the excitation spectra at all, which indicated that emission arose from a charge-transfer state.<sup>[15]</sup>

Considering the polarity-dependent optical properties of **PM1**–**PM3** and rich lineage of DCV derivatives in photovoltaic systems, piperazine–DCV conjugates were expected to be endowed with AIE attributes. To understand aggregation behav-

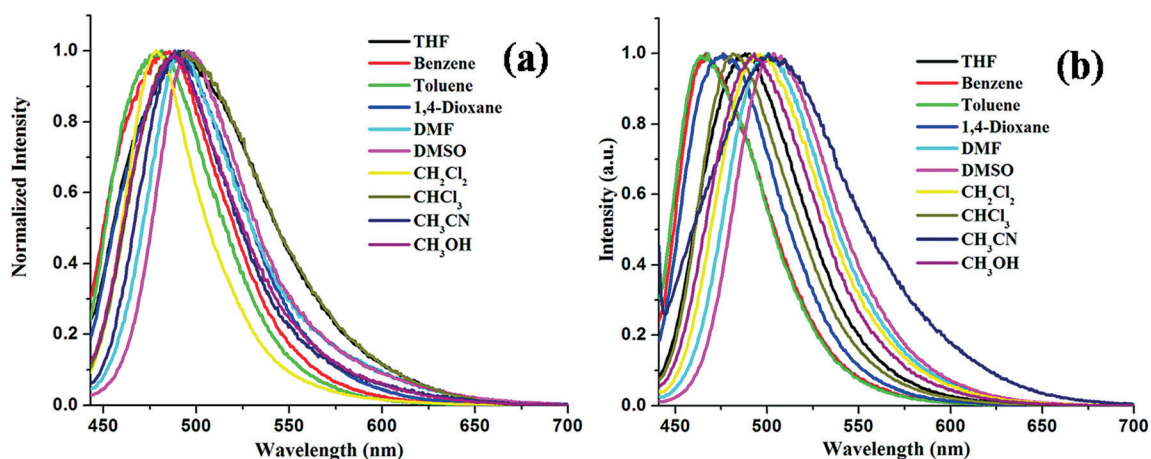


Figure 1. Emission spectra of **PM2** (a) and **PM3** (b) in solvents of varying polarity ( $c=5 \times 10^{-5}$  molL $^{-1}$ ).

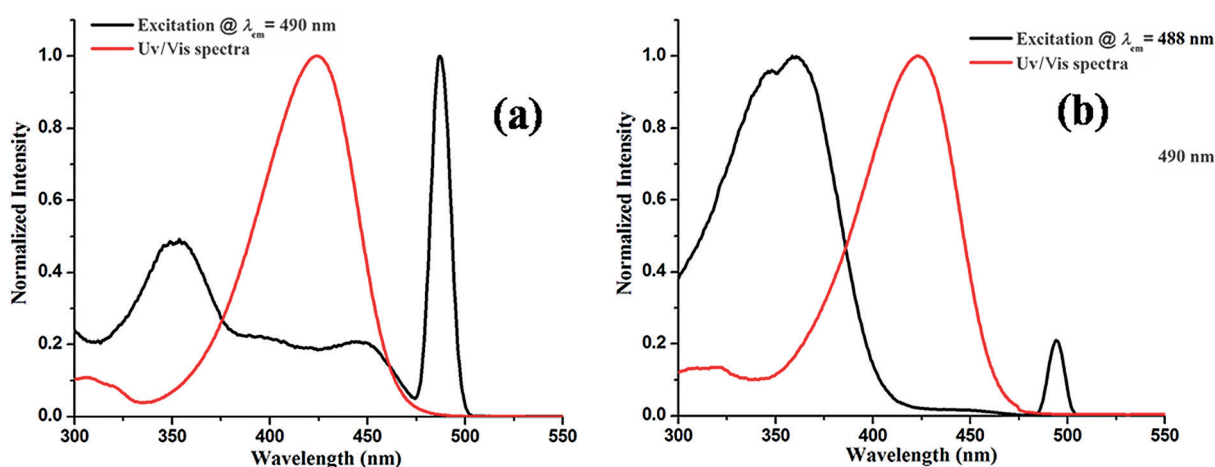


Figure 2. Excitation spectra of **PM2** (a) and **PM3** (b) at  $\lambda_{em}=488$  and  $494$  nm, respectively.

ior, the absorption and emission properties of **PM1–PM3** were examined in mixtures of THF/water with varying compositions; water is a poor solvent for these compounds and must promote the aggregation process.

Compounds **PM2** and **PM3** produced analogous absorption spectra with increasing water fraction ( $f_w$ ), whereas **PM1** displayed insignificant changes (Figure S7 in the Supporting Information). Compounds **PM2** and **PM3** do not show major changes up to  $f_w=70\%$ , but as  $f_w$  reaches  $80\%$ , a dramatic decrease in the absorption intensity is observed for the band at  $\lambda \approx 423$  nm. At  $f_w=90\%$ , a leveling-off tail appeared in the visible region, which might be due to the Mie scattering effect commonly observed in nanoaggregate suspensions.<sup>[16]</sup>

To monitor the excited-state behavior of the compounds during aggregation, photoluminescence spectra were acquired by using same solvent composition (Figure 3 and Figure S10 in the Supporting Information). Compound **PM1** displayed properties similar to an ACQ luminogen (Figure S8 in the Supporting Information). The addition of water to **PM2** up to  $f_w=80\%$  produced a continuous decrease in fluorescence intensity for the band at  $\lambda=488$  nm, and at  $f_w=90\%$  a redshifted band

emerged at  $\lambda=525$  nm, which further strengthened at  $f_w=100\%$ . It is noteworthy to mention that at  $f_w=100\%$ , along with the major band at  $\lambda=525$  nm, a shoulder appeared at  $\lambda=564$  nm. On the other hand, compound **PM3** manifested an overall quenching of the emission intensity up to  $f_w=80\%$  for the band at  $\lambda=494$  nm. At  $f_w=90\%$ , a new band started to appear at  $\lambda=580$  nm, along with a native emission band at  $\lambda=494$  nm. A dramatic fluorescence enhancement for the band at  $\lambda=580$  nm was observed at  $f_w=100\%$ , with complete loss of the original band at  $\lambda=488$  nm.

The exact THF/water ratio for maximum fluorescence enhancement can only be perceived by stepwise monitoring of the fluorescence intensity as a function of  $f_w$ . The emission spectra of **PM2** and **PM3** (Figure 4) were thus acquired at  $f_w=92, 94, 96, 98,$  and  $100\%$ . For **PM2**, as the water content increased to  $f_w=90\%$  a new band appeared at  $\lambda=525$  nm with slightly enhanced fluorescence. Interestingly, upon increasing to  $f_w=92\%$ , along with the band at  $\lambda=525$  nm, a shoulder appeared at  $\lambda=564$  nm. Both bands intensified and attained maxima at  $f_w=96\%$ . Further addition of water ( $f_w=98$  and  $100\%$ ) severely quenched the emission due to apparent pre-

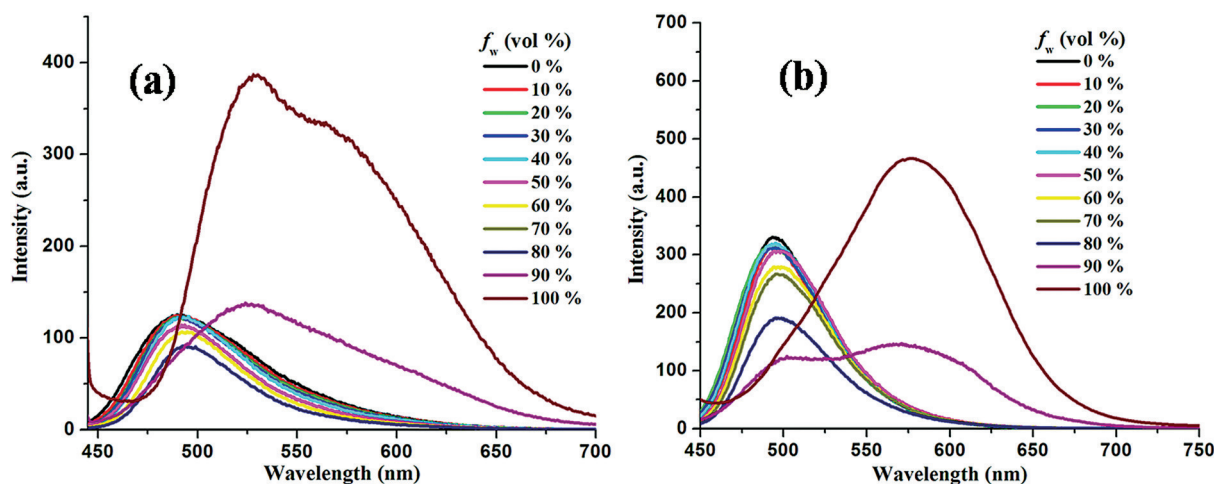


Figure 3. Emission spectra of PM2 (a) and PM3 (b) in mixtures of THF/water with different water volume fractions ( $c = 5 \times 10^{-5} \text{ mol L}^{-1}$ )

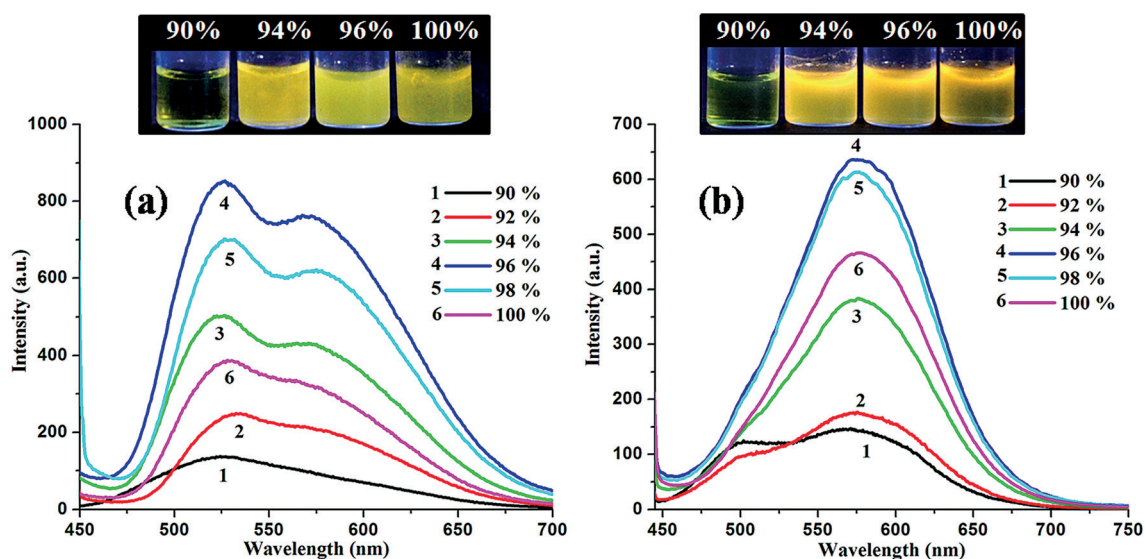


Figure 4. Emission spectra of PM2 (a) and PM3 (b) in mixtures of THF/water from  $f_w = 90$  to 100% ( $c = 5 \times 10^{-5} \text{ mol L}^{-1}$ ).

precipitation. Compound **PM3** displayed a dissimilar emission profile with increasing  $f_w$ . As the water content exceeded 90%, the band at  $\lambda = 494 \text{ nm}$  diminished and that at  $\lambda = 580 \text{ nm}$  became the major band and attained a maximum at  $f_w = 96\%$ . Upon further increasing the water content, the emission intensity lowered possibly due to decreased solubility and precipitation.<sup>[17b]</sup> Both **PM2** and **PM3** showed outstanding fluorescence enhancement ( $\approx 8$  and  $\approx 2.5$  times) upon aggregation, and thus, can easily be categorized as AIE-active luminogens.

To evaluate the process of aggregate buildup and its effect on emission enhancement, we attempted to determine the nature of the ensuing aggregates. We examined the powder XRD patterns (Figure S13 in the Supporting Information) for aggregates of **PM2** and **PM3** at  $f_w = 90$  (water fraction for the onset of aggregation) and 96% (water fraction for maximum emission enhancement). The powder XRD patterns suggested the purely amorphous nature of nascent aggregates formed at  $f_w = 90\%$ , whereas the well-defined peaks in the powder XRD patterns of **PM2** and **PM3** at  $f_w = 96\%$  suggested crystalline

nature of the aggregates at the point of maximum emission enhancement. These observations advocated that the aggregates of **PM2** and **PM3** leading to maximum emission enhancement at  $f_w = 96\%$  possessed a certain degree of crystallinity.

#### Mechanism of AIE and substituent effects

Fascinating optical properties of **PM2** and **PM3** observed upon aggregation and variation of the fluorescence with solvent polarity prompted us to elucidate the most probable mechanism of AIE. If RIR is the major route for emission enhancement, it should be proven experimentally. It is well documented that AIE-active luminogens relying on RIR exhibit fluorescence enhancement upon increasing viscosity of the solution.<sup>[17]</sup> To affirm this, the emission spectra of **PM2** and **PM3** were acquired in a mixture of methanol/glycerol ( $c = 5 \times 10^{-5} \text{ mol L}^{-1}$ , 0.2 vol % THF) of varying composition (Figure 5a and b). It was observed that both **PM2** and **PM3** showed tremendous in-

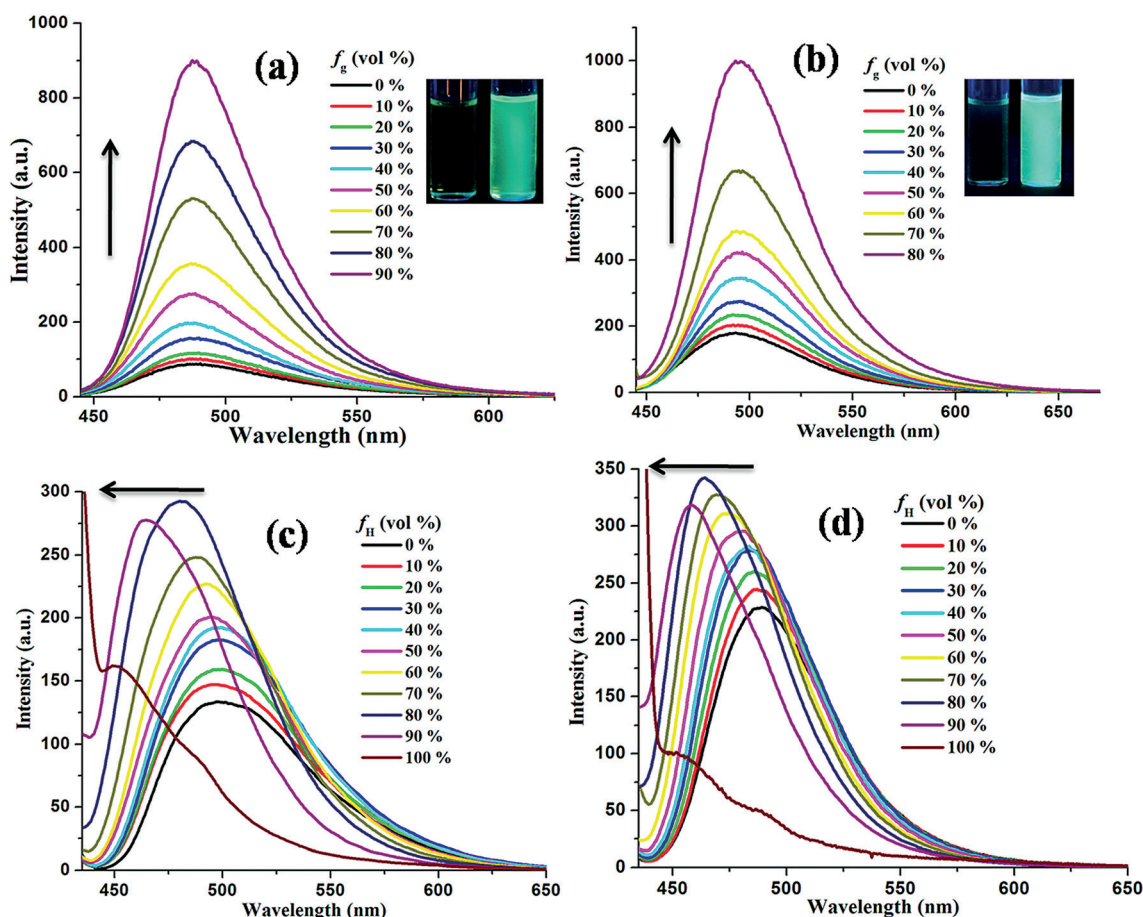


**Figure 5.** Emission spectra of **PM2** with increasing fractions of glycerol (a) and hexane (c), and emission spectra of **PM3** with increasing fractions of glycerol (b) and hexane (d) ( $c = 5 \times 10^{-5} \text{ mol L}^{-1}$ ).

creases in emission intensity with increasing glycerol content. Compound **PM2** displayed about eight times enhancement in emission intensity at a glycerol fraction ( $f_g$ ) of 90%, whereas **PM3** manifested about six times enhancement (at  $f_g$  80%). There was no apparent change in the position of emission maxima at  $\lambda = 488$  and  $494$  nm for **PM2** and **PM3**, respectively. This eliminated the possibility of fluorescence enhancement due to aggregation and established that observed changes were solely due to the viscosity effect. Thus, viscosity-dependent fluorescence enhancement confirmed the involvement of RIR in the AIE process.

Compounds **PM2** and **PM3** exhibited solvatochromism and quenching of the emission intensity up to  $f_w = 90\%$  with red-shifted emission maxima, which raised the possibility of TICT. It was reported previously that, if TICT was involved in the AIE mechanism, the systems would undergo a blueshift and appreciable fluorescence enhancement with increasing hexane ratio.<sup>[18]</sup> Hexane is a nonpolar solvent; therefore, upon adding small portions of hexane, there should be an increase in the fluorescence intensity. Because hexane is a poor solvent for **PM2** and **PM3**, larger fractions of hexane should lead to AIE in these compounds. To further confirm this phenomenon, the emission spectra of **PM2** and **PM3** were monitored in a mixture of THF/hexane by varying the hexane fractions. Upon increasing the hexane fraction,  $f_H$ , there is an apparent blueshift in

the emission maxima of **PM2** and **PM3** (Figure 5c and d). As  $f_H$  reached 100%, compounds **PM2** and **PM3** produced total blueshifts of 30 and 32 nm, respectively. However, the emission intensity was affected differently. There were increases in the emission intensities of **PM2** and **PM3** up to  $f_H = 80\%$ ; further addition of hexane ( $f_H = 90$  and  $100\%$ ) led to a decrease in fluorescence intensity. As expected, the subsequent addition of hexane up to  $f_H = 80\%$  led to emission enhancement, which was previously due to TICT and later due to RIR. At higher  $f_H$  (90 and 100%), quenching was induced by precipitation due to poor solubility of the compounds in hexane.

TICT and RIR are competitive processes and affect the AIE attributes differently. The vivid optical response during aggregation can be explained as follows: As  $f_w$  increases stepwise, fluorescence quenching, with a redshift in the emission maxima, is observed up to  $f_w = 90\%$ , which is an immediate consequence of TICT because the addition of water increases the polarity of the system. At  $f_w > 90\%$ , RIR becomes important and weakens TICT to induce fluorescence enhancement due to aggregation.<sup>[17b,19]</sup>

The time-resolved emission decay profiles for **PM2** and **PM3** have also been examined in a mixture of THF/water with varying water contents (Figure 6). Different decay dynamics for **PM2** and **PM3** with varying water fractions rationalized their diverse emission behavior. Up to  $f_w = 80\%$ , the average lifetime

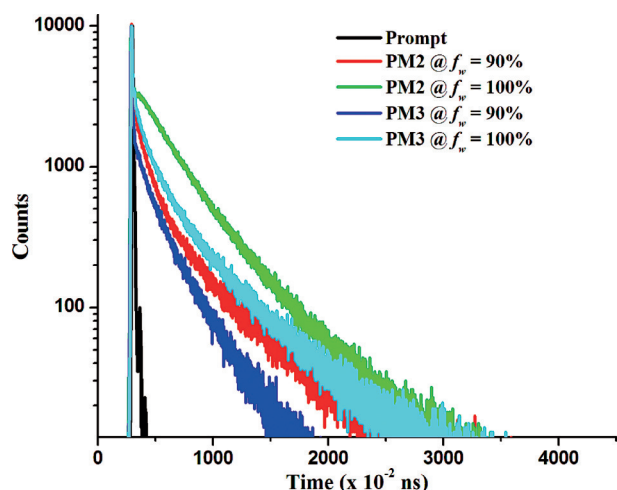


**Figure 6.** A logarithmic view of the time-resolved fluorescence of **PM2** and **PM3** at varying  $f_w$ .

( $\tau_{av}$ ) was very small and beyond the detection limit of the instrument. As the water content rose to  $f_w = 90$  and  $100\%$ , a significant increase in  $\tau_{av}$  occurred for **PM2** and **PM3**. The  $\tau_{av}$  values were 2.66 and 4.85 ns for **PM2** at  $f_w = 90$  and  $100\%$ , respectively; the  $\tau_{av}$  values for **PM3** were slightly lower: 2.59 and 3.29 ns at  $f_w = 90$  and  $100\%$ , respectively. The increased lifetime at higher water fractions indicated decreased nonradiative decay, which again substantiated competitive TICT and RIR processes. Increasing water fractions raise the polarity of the media and support the occurrence of TICT; a “dark state” characterized by fast nonradiative decay and decreased lifetime, leading to fluorescence quenching. Active intramolecular rotations are restricted by aggregation at higher water fractions, which effectively prevent formation of the dark state, leading to enhanced emission with a longer lifetime.

The difference in the emission behavior of **PM2** and **PM3** with increasing water gradient also accounted for the aforementioned mechanism. Compound **PM3** possesses a pyrimidyl group as  $A'$ , which is clearly more electron withdrawing than the pyridyl moiety in **PM2**. Hence, TICT is more pronounced in **PM3** and results in a more redshifted emission with smaller  $\tau_{av}$  value (2.59 and 3.29 ns) than that of **PM2** (2.66 and 4.85 ns) upon aggregation. RIR does not remain as effective in **PM3** as that in **PM2** due to a more effective TICT, which leads to only about 2.5 times emission enhancement in **PM3** relative to about 8 times in **PM2** upon aggregation. Moreover, more proficient solvatochromism in **PM3** than that in **PM2** suggested the same mechanism.

### Solid-state emission properties

The photoluminescence spectra of **PM1–PM3** have also been acquired in the solid state (Figure 7). Compounds **PM2** and **PM3** displayed a broad spectral range from  $\lambda = 481$  to  $700$  nm when excited at  $\lambda \approx 423$  nm. Compound **PM1**, on the other hand, did not show any emission. The solid-state emission profiles and emission colors of **PM2** and **PM3** were almost identical to those of the aggregated state. Visibly, the solid-state emission color of **PM2** was green–yellow and a bit lighter than yellow–orange for **PM3**, which could be related to more redshifted spectra of aggregates of **PM3** (see above).

Because the powder XRD patterns suggested the crystalline nature of the aggregates, the emission behavior of these molecules in the crystalline state should also be monitored. Although we could not obtain diffraction-quality crystals of the compounds, gradual evaporation of the solution of aggregate at  $f_w = 100\%$  over a period of 2–3 days led to very fine crystalline fibers of **PM2** and **PM3**. The crystalline fibers were fluorescent under UV illumination ( $\lambda_{ex} = 365$  nm); the respective

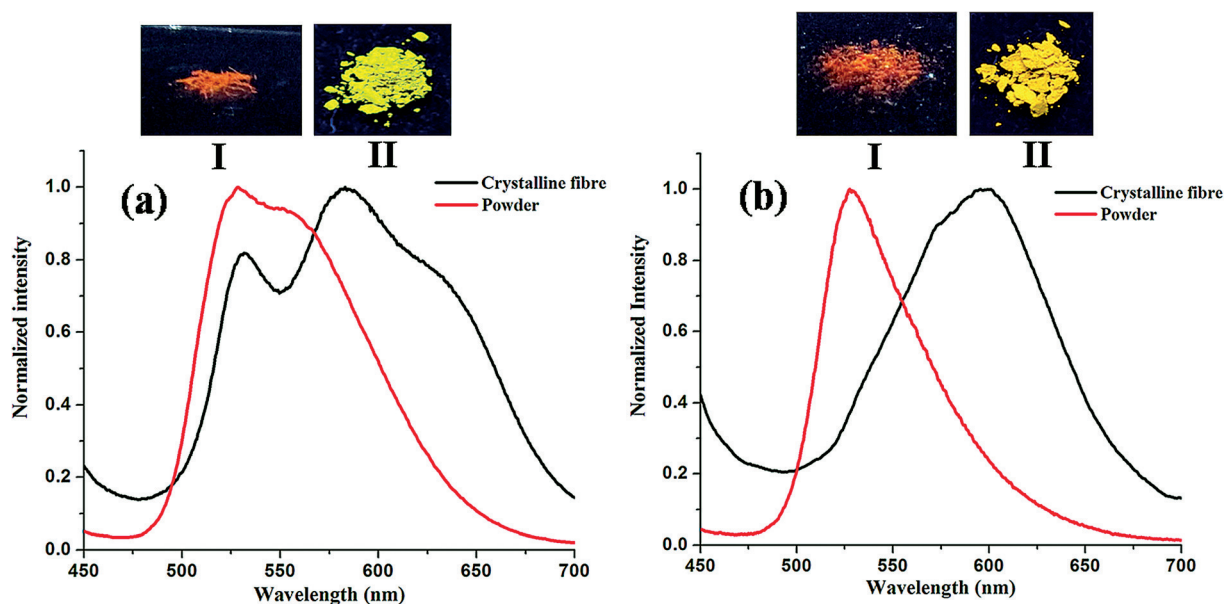


**Figure 7.** Solid-state emission spectra of **PM2** (a) and **PM3** (b). Inset: images of crystalline fiber (I) and solid powder (II) of **PM2** (a) and **PM3** (b) under UV illumination ( $\lambda_{ex} = 365$  nm).

images of crystalline fibers and powders under UV illumination are depicted in Figure 7 (insets). It can be seen that the fluorescence of the crystalline fibers is redshifted relative to those of the solid powders. For further verification, we acquired solid-state emission spectra of the crystalline fibers of **PM2** and **PM3** (Figure 7). In the solid-state emission spectrum, the crystalline fibers of **PM2** displayed two bands at  $\lambda = 531$  and  $583$  nm, along with a shoulder at  $\lambda \approx 631$  nm, whereas that of **PM3** displayed a single band at  $\lambda = 600$  nm. It is clear that partial crystallization induces a redshift in the emission maxima of **PM2** and **PM3**. The redshifts in the emission maxima of **PM2** and **PM3**, from solution to crystalline fibers through aggregates, are 95 and 106 nm, respectively. In other words, it can be concluded that, upon onset of aggregation at  $f_w = 90\%$ , a further increase in water content enables the aggregates to acquire an ordered structure through increased intermolecular interactions, which are also accountable for the aforementioned redshifts.

### Aggregate morphology

Because we focused our attention toward the development of 1D nanostructures that exhibited AIE, we verified our assumptions in practice by subjecting the aggregates to SEM, TEM, and fluorescence microscopy. Compounds **PM2** and **PM3** both provided 1D nanoaggregates with different morphologies. SEM data revealed that **PM2** consisted of perfect leaf-shaped aggregates, while **PM3** formed twisted ribbon-like nanoaggregates (Figure 8a and Figure S11a in the Supporting Information). A closer view of the SEM images of aggregates of **PM3** showed a unique morphology, wherein twisted ribbons actually converged at a point to fabricate the flower-shaped edifice (Figure 8c and Figure S11c in the Supporting Information). Notably, compound **PM3** displayed more than one hierarchical assembly. As shown in Figure 8c, there are some straight ribbons along with a couple of helical fibers. It is believed that the twisted ribbons braid together to form helical fibers (Figure S11 in the Supporting Information).<sup>[20]</sup>

TEM data confirmed the self-assembly of the aggregates. Branching in the leaf-shaped aggregates of **PM2** can be visual-

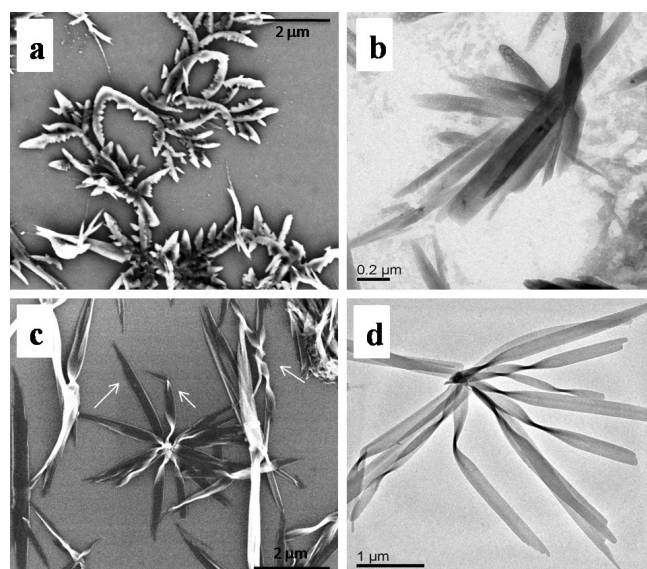


**Figure 8.** SEM (a, c) and TEM (b, d) images of the aggregates of **PM2** (a, b) and **PM3** (c, d) formed in a mixture of THF/water ( $f_w = 90\%$ ;  $c = 5 \times 10^{-5} \text{ mol L}^{-1}$ ).

ized in Figure 8b and d and Figure S11b and d in the Supporting Information. For **PM3**, TEM data revealed the occurrence of more than one twist in each ribbon-shaped structure. These twists also support the formation of helical fibers as one of the hierarchical assemblies. Fluorescence microscopy images of both **PM2** and **PM3** (Figure 9 and Figure S12 in the Supporting Information) display dichromic fluorescence under blue or green excitation. An overlay of the images produced a yellow-colored image of the respective aggregates (Figure 9c), and thus, suggested that dichromic fluorescence originated from a single entity, namely, a leaf-shaped aggregate in **PM2** and flower-like aggregates in **PM3**.

### Crystal structure

Furthermore, to gain a deeper insight into the aggregation process and to rationalize the concomitant relationship between molecular packing and aggregate morphology, we tried

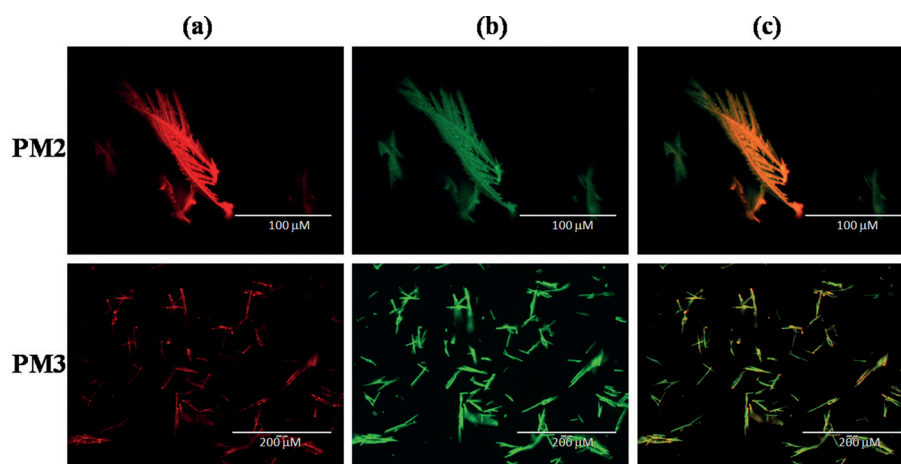


**Figure 9.** Fluorescence microscopy images of **PM2** and **PM3** under red (a) and green (b) excitation, as well as overlaid images (c).

to obtain single crystals of **PM1**–**PM3** by slow diffusion of  $\text{CH}_2\text{Cl}_2/\text{CH}_3\text{OH}$  into a solution of the respective compound. Fortunately, we obtained crystals of **PM3**, which crystallizes in the triclinic system with the  $P\bar{1}$  space group. Data collection and refinement parameters for **PM3** are gathered in Table S1 in the Supporting Information, selected geometric parameters can be found in Table S2 in the Supporting Information, and a pertinent view is depicted in Figure 10. It is evident from the crystal structure that the piperazine unit acquires a chair conformation. The dihedral angle between piperazine (N4, C6, C5, N3, C8, C7) and the pyrimidine (C1, N1, C4, C3, C2, N2) core is  $17.80^\circ$  and between piperazine and the phenyl (C9, C10, C11, C12, C13, C14) core is  $9.76^\circ$ . Selection of the piperazine unit as a spacer was instrumental, since it is now clear from the crystal structure that the molecule acquires a twisted conformation due to torsions offered by the piperazine unit.

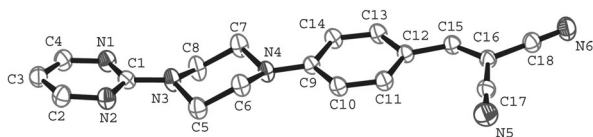


**Figure 10.** ORTEP view of **PM3**; ellipsoids are given at the 30% probability level (hydrogen atoms are omitted for clarity).

Careful examination of the crystal packing in **PM3** revealed that each molecule was surrounded by three neighboring molecules, mainly through  $\text{C}\cdots\text{H}\cdots\text{N}$  bonding interactions (Figure 11). Molecular packing through these interactions unveiled that DCV units of the adjacent molecules stacked in a slightly slipped manner through face-to-face  $\text{C}\cdots\text{H}\cdots\text{N}$  interactions (2.715 Å). Of two other  $\text{C}\cdots\text{H}\cdots\text{N}$  interactions, one involves the piperazine hydrogen and DCV nitrogen atom of one adjacent molecule, whereas the other is between the piperazine hydrogen and DCV nitrogen atom of a neighboring molecule. These interactions, with bond lengths of 2.722 and 2.603 Å, enable the molecules to be arranged in an almost head-to-tail manner, analogous to J aggregates (Figure 11 c).<sup>[21]</sup> The comparatively short length of these interactions leads to strongly coupled aggregate structures and also reflects possible electronic communication between these molecules to promote the redshift upon aggregation or in the solid state.<sup>[22]</sup> The aforementioned interactions facilitate 1D self-assembly in **PM3** and make the twisted structure rigid. Thus, these hydrogen-bonding interactions restrict intramolecular rotations and lead to enhanced emission in the solid state. DFT studies revealed almost identical structures for **PM1** and **PM2**, which compensated for the unavailability of crystal structures of these compounds (Figure S14 in the Supporting Information)

### Electrochemical studies

The electronic structures of luminogens play a pivotal role in determining charge-transfer processes and also provide an account of the HOMO and LUMO energy levels of the molecules.

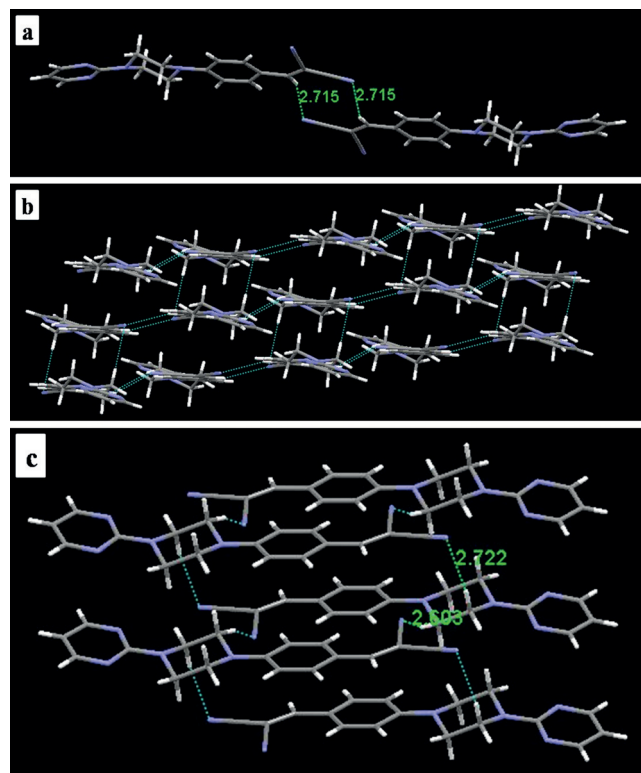


**Figure 11.** Crystal packing in **PM3** through face-to-face  $\text{C}\cdots\text{H}\cdots\text{N}$  interactions (a). Packing in **PM3** through all  $\text{C}\cdots\text{H}\cdots\text{N}$  hydrogen-bonding interactions (b), displaying a wavy 1D structure and head-to-tail packing in **PM3** (c).

Cyclic voltammograms of these molecules were acquired in acetonitrile ( $c=1\times 10^{-4}\text{ mol L}^{-1}$ ). In the cyclic voltammogram (Figure 12), compound **PM1** showed a reversible oxidation wave, whereas **PM2** and **PM3** displayed irreversible oxidation waves (weaker in **PM3**), which may arise due to the formation of a stable radical cation in the conjugated sequence. The difference in the oxidation behavior can be rationalized by the substituent effect. The reversibility of the oxidation curve in **PM1** suggested that the radical cation for this system was more stable than those of **PM2** and **PM3**. This corresponded well with the electron-donating ability of the ethyl group in **PM1**, whereas the pyridyl (**PM2**) and pyrimidyl (**PM3**) moieties act as electron-withdrawing groups. These compounds (**PM1**–**PM3**) displayed an irreversible reduction wave in their cyclic voltammograms, which marked the formation of radical anions at the terminal DCV unit. Experimental HOMO and LUMO energies were evaluated from the oxidation and reduction potentials, respectively (**PM1**:  $E=-5.68\text{ eV}$  (HOMO),  $E=-3.20\text{ eV}$  (LUMO); **PM2**:  $E=-5.57\text{ eV}$  (HOMO),  $E=-3.23\text{ eV}$  (LUMO); **PM3**:  $E=-5.59\text{ eV}$  (HOMO),  $E=-3.24\text{ eV}$  (LUMO); Table 1). The HOMO is more stabilized in **PM1**, but the LUMO is more stabilized in **PM2** and **PM3**, which is in good agreement with the electron-donating ability of the ethyl substituent and -withdrawing ability of the pyridyl and pyrimidyl substituents. The HOMO–LUMO gaps (**PM1**, 2.48 eV; **PM2**, 2.34 eV; **PM3**, 2.35 eV; Table 1) were also calculated and found to be in good agreement with those obtained from absorption studies.

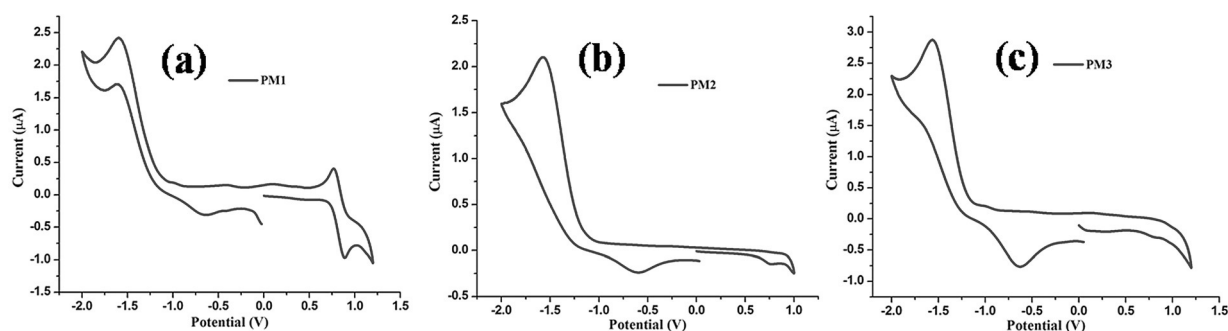


Figure 12. Cyclic voltammograms of **PM1** (a), **PM2** (b), and **PM3** (c) in acetonitrile ( $c = 5 \times 10^{-5} \text{ mol L}^{-1}$ ).

	LUMO		HOMO		$V_{CV}$	$E_g$	
	$V_{CV}$	$V_{calcd}$	$V_{CV}$	$V_{calcd}$		$V_{calcd}$	$V_{UV}$
<b>PM1</b>	-3.20	-2.37	-5.68	-5.82	2.48	3.46	2.91
<b>PM2</b>	-3.23	-2.42	-5.57	-5.82	2.34	3.40	2.92
<b>PM3</b>	-3.24	-2.42	-5.59	-5.85	2.35	3.43	2.93

### Theoretical considerations

The electronic structures of **PM1–PM3** were further appraised by means of DFT (B3LYP 6-31G\*) and the resulting molecular orbital distributions of the frontier orbitals are depicted in Figure 13. Calculated energy levels and HOMO–LUMO gaps are summarized in Table 1. The computational results indicated that in **PM1–PM3** the HOMO was spread over whole molecule,

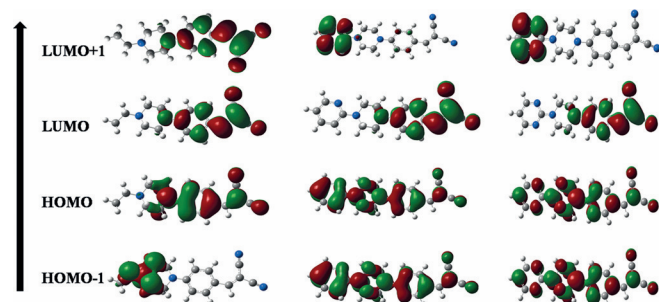


Figure 13. Frontier molecular orbitals of **PM1** (left), **PM2** (middle), and **PM3** (right) obtained from DFT calculations.

whereas the LUMO was mainly attributed to the aryl-DCV moiety, which was consistent with the strong accepting tendency of cyano groups. Notably, there is no contribution to the LUMO by  $A'$  groups, that is, pyridyl in **PM2** and pyrimidyl in **PM3**. It is presumed that the presence of two acceptors creates competition, wherein DCV, which is the better acceptor, excels.

To confirm this assumption, we also evaluated the molecular orbital distribution of HOMO-1 and LUMO + 1. The HOMO-1 is very similar to that of HOMO and spread over the whole molecule, whereas LUMO + 1 is only associated with  $A'$  (pyridyl and

pyrimidyl). It can further be added that charge-transfer transitions are not contributed to by HOMO–LUMO alone, but other possible transitions involving HOMO-1 and LUMO + 1 make a significant contribution. The HOMO–LUMO transition corresponds to the main absorption band at  $\lambda \approx 423 \text{ nm}$  in both **PM2** and **PM3**. The broad absorption in these compounds revealed the involvement of other transitions of comparable energies. These observations account well for the competitive behavior of the two acceptor groups. The effect of  $A'$  can be realized particularly on the LUMO level because it was stabilized to a greater extent in **PM3** and **PM2** than that in **PM1**. Theoretical results also supported the band gap values for **PM1–PM3** through electrochemical and UV/Vis observations. Time-dependent (TD) DFT calculations were also performed on **PM1–PM3**, and the UV/Vis spectra obtained theoretically were comparable to those obtained experimentally (Figure S15 in the Supporting Information).

### Conclusion

Through this work, a highly ambitious approach has been developed to obtain interesting 1D nanostructures with AIE attributes and solid-state emission. In this context, we used three rationally designed, and effortlessly synthesized, simple compounds that were composed of piperazine/DCV derivatives to offer symmetric (**PM1**) and asymmetric (**PM2**, **PM3**) D–A constructs. Asymmetry was achieved by decorating the compounds with  $A'$  (pyridyl, pyrimidyl) groups. Surprisingly, the symmetric D–A molecule was AIE-inactive, whereas asymmetric D–A molecules were endowed with AIE activity, solvatochromism, viscochromism, and strong solid-state emissions, which clearly justified the key role of  $A'$  in triggering AIE in these compounds. The mechanism for these intriguing properties was established to be under the competitive control of TICT and RIR, which also suggested that optical variations in **PM2** and **PM3** could be directly related to the comparative acceptor strength of  $A'$ . Flexibility provided by the piperazine moiety and intermolecular hydrogen-bonding interactions led to exquisite 1D nanostructures. The outcomes of this study are encouraging for the design of new, improved, AIE-active lumino-phores by exploiting asymmetry in the structures.

## Experimental Section

### Reagents

The solvents were dried and distilled prior to use by following standard procedures.<sup>[23]</sup> 1-Ethylpiperazine, 1-(2-pyridyl)piperazine, 1-(2-pyridyl)piperazine, and malononitrile were procured from Sigma Aldrich India and used as received without further purifications. The aldehydes **1a–c** were prepared by following a procedure reported in the literature.<sup>[13]</sup>

### General methods

Elemental analyses for C, H, and N were obtained on an Elementar Vario EL III Carlo Erba 1108 analyzer from the microanalytical laboratory of the Sophisticated Analytical Instrumentation Facility (SAIF), Central Drug Research Institute (CDRI), Lucknow, India. Electronic absorption spectra were acquired on Shimadzu UV-1601 spectrophotometers. <sup>1</sup>H and <sup>13</sup>C spectra were acquired on a JEOL AL 300 FT-NMR spectrometer by using Si(CH<sub>3</sub>)<sub>4</sub> as an internal reference. Fluorescence spectra (95% aqueous methanol) at room temperature were acquired on a PerkinElmer LS 55 fluorescence spectrometer. SEM images were acquired on a JEOL JSM 840A scanning electron microscope. TEM images were obtained on a FEI Technai 20 U twin transmission electron microscope. Fluorescence microscopic images were recorded on an EVOS FL cell imaging system. High-resolution mass spectra were recorded on a Bruker-Daltonics micrOTOF-Q II mass spectrometer. Cyclic voltammetry measurements were performed on a CHI 620c electrochemical analyzer at RT. Experiments were performed in an air-tight single-compartment cell by using platinum wire as the counter electrode, a glassy carbon working electrode, and an Ag/Ag<sup>+</sup> reference electrode. Crystal data for **PM3** was collected on a Bruker Kappa Apex-II diffractometer at RT with Mo<sub>Kα</sub> radiation (λ = 0.71073 Å). The structure was solved by direct methods (SHELXS 97) and refined by full-matrix least-squares on F<sup>2</sup> (SHELX 97).<sup>[24]</sup> Non-hydrogen atoms were refined with anisotropic thermal parameters. Hydrogen atoms were geometrically fixed and refined by using a riding model. The computer program PLATON was used for analyzing interactions and stacking distances.<sup>[25]</sup>

CCDC 1418259 contains the supplementary crystallographic data for this paper. These data are provided free of charge by The Cambridge Crystallographic Data Centre.

### Synthesis of PM1

In a round-bottom flask, compound **1a** (0.500 g, 2.29 mmol) and malononitrile (0.152 g, 2.29 mmol) were dissolved in ethanol (15 mL). To this solution, catalytic amounts of piperidine (1–2 drops) was added and mixture was stirred at room temperature for 1.5 h. After completion of the reaction, a yellow precipitate appeared, which was filtered, washed with water, and dried in a vacuum to afford **PM1** as a bright-yellow solid (0.349 g, 70%). <sup>1</sup>H NMR (CDCl<sub>3</sub>): δ = 1.31 (t, 3H; methyl), 3.14 (s, 8H; piperazine), 3.82 (s, 2H; methylene), 6.67 (s, 2H; phenyl), 7.46 (s, 1H; methine), 7.80 ppm (s, 2H; phenyl); <sup>13</sup>C NMR (CDCl<sub>3</sub>): δ = 40.1, 111.6, 115.4, 133.8, 158.8 ppm; HRMS: *m/z* calcd for C<sub>16</sub>H<sub>18</sub>N<sub>4</sub> [M+H]<sup>+</sup>: 267.1583; found: 267.1604; elemental analysis calcd (%) for C<sub>16</sub>H<sub>18</sub>N<sub>4</sub>: C 72.15, H 6.81, N 21.04; found: C 72.10, H 6.75, N 21.0.

### Synthesis of PM2

Compound **PM2** was prepared by following the same procedure as that used for **PM1** with **1b** (0.5 g, 1.88 mmol) in place of **1a**.

Yield: 0.438 g, 88%; <sup>1</sup>H NMR (CDCl<sub>3</sub>): δ = 6.66 (t, 1H; pyridyl), 6.84, (d, *J* = 8.7 Hz, 1H; pyridyl), 7.10 (d, *J* = 9.0 Hz, 2H; phenyl), 7.54 (d, *J* = 6.9 Hz, 1H; methine), 7.86 (d, *J* = 8.7 Hz, 2H; phenyl), 8.10 ppm (s, 1H; pyridyl); <sup>13</sup>C NMR (CDCl<sub>3</sub>): δ = 43.7, 43.4, 70.4, 107.0, 113.0, 115.2, 120.0, 133.6, 137.6, 147.5, 154.1, 158.8 ppm; HRMS: *m/z* calcd for C<sub>19</sub>H<sub>17</sub>N<sub>5</sub> [M+H]<sup>+</sup>: 316.1552; found: 316.1551; elemental analysis calcd (%) for C<sub>19</sub>H<sub>17</sub>N<sub>5</sub>: C 72.36, H 5.43, N 22.21; found: C 72.29, H 5.39, N 22.19.

### Synthesis of PM3

Compound **PM3** was prepared by following the same procedure as that used for **PM1** with **1c** (0.5 g, 1.87 mmol) in place of **1a**. Yield: 0.451 g, 90%; <sup>1</sup>H NMR (CDCl<sub>3</sub>): δ = 3.60 (t, 4H; piperazine), 4.01 (t, 4H; piperazine), 6.57 (t, 1H; pyrimidyl), 6.89 (d, *J* = 8.7 Hz, 2H; phenyl), 7.50 (s, 1H; methine), 7.84 (d, *J* = 9.0 Hz, 2H; phenyl), 8.35 ppm (s, 2H; pyrimidyl); <sup>13</sup>C NMR (CDCl<sub>3</sub>): δ = 25.1, 43.0, 46.2, 92.3, 113.2, 133.7, 139.6, 154.3, 157.8 ppm; HRMS: *m/z* calcd for C<sub>19</sub>H<sub>17</sub>N<sub>5</sub> [M+H]<sup>+</sup>: 317.1504; found: 317.1509; elemental analysis calcd (%) for C<sub>18</sub>H<sub>16</sub>N<sub>6</sub>: C 68.34, H 5.10, N 26.56; found: C 68.29, H 5.05, N 26.48.

### Theoretical studies

Quantum chemical calculations were performed at the B3LYP DFT level by using B3LYP/6-31G\*\* for **PM1–PM3**.<sup>[17b]</sup> All geometry optimizations and frequency calculations (to verify a genuine minimum-energy structure) were performed by using the Gaussian 09 suite of programs.<sup>[26]</sup>

### Acknowledgement

We acknowledge financial support from the Department of Science and Technology (DST), New Delhi, through the scheme SR/S1/IC-25/2011. R.S.S. acknowledges the University Grants Commission, New Delhi, India, for a Senior Research Fellowship (19-12/2010(i) EU-IV).

**Keywords:** aggregation • donor–acceptor systems • fluorescence • nanostructures • self-assembly

- [1] a) C. F. J. Faul, *Acc. Chem. Res.* **2014**, *47*, 3428–3438; b) D. Gentili, F. Valle, C. Albonetti, F. Liscio, M. Cavallini, *Acc. Chem. Res.* **2014**, *47*, 2692–2699; c) R. M. Parker, J. Zhang, Y. Zheng, R. J. Coulston, C. A. Smith, A. R. Salmon, Z. Yu, O. A. Scherman, C. Abell, *Adv. Funct. Mater.* **2015**, *25*, 4091–4100; d) F. Pu, L. Wu, E. Ju, X. Ran, J. Ren, X. Qu, *Adv. Funct. Mater.* **2014**, *24*, 4549–4555; e) Y. Liu, Y. Liu, J. J. Yin, Z. Nie, *Macromol. Rapid Commun.* **2015**, *36*, 711–725.
- [2] a) L. Maggini, D. Bonifazi, *Chem. Soc. Rev.* **2012**, *41*, 211–241; b) S.-J. Yoon, J. H. Kim, K. S. Kim, J. W. Chung, B. Heinrich, F. Mathevet, P. Kim, B. Donnio, A. J. Attias, D. Kim, S. Y. Park, *Adv. Funct. Mater.* **2012**, *22*, 61–69; c) E. Lee, B. Hammer, J.-K. Kim, Z. Page, T. Emrick, R. C. Hayward, *J. Am. Chem. Soc.* **2011**, *133*, 10390–10393; d) D.-J. Hong, E. Lee, M. Lee, *Chem. Commun.* **2007**, 1801–1803; e) Z. Huang, E. Lee, H.-J. Kim, M. Lee, *Chem. Commun.* **2009**, 6819–6821; f) A. Wicklein, S. Ghosh, M. Sommer, F. Wurthner, M. Thelakkat, *ACS Nano* **2009**, *3*, 1107; g) J. Xiao, B. Yang, J. I. Wong, Y. Liu, F. Wei, K. J. Tan, X. Teng, Y. Wu, L. Huang, C. Kloc, F. Boey, J. Ma, H. Zhang, H. Y. Yang, Q. Zhang, *Org. Lett.* **2011**, *13*, 3004–3007.
- [3] a) J. Luo, Z. Xie, J. W. Y. Lam, L. Cheng, H. Chen, C. Qiu, H. S. Kwok, X. Zhan, Y. Liu, D. Zhu, B. Z. Tang, *Chem. Commun.* **2001**, 1740–1741; b) Y. Hong, J. W. Y. Lam, B. Z. Tang, *Chem. Soc. Rev.* **2011**, *40*, 5361–5388.
- [4] a) G. Iasilli, A. Battisti, F. Tantussi, F. Fusco, M. Allegrini, G. Ruggeri, A. Pucci, *Macromol. Chem. Phys.* **2014**, *215*, 499–506; b) R. Hu, C. F. A. G.

- Durán, J. W. Y. Lam, J. L. B. Vázquez, C. Deng, S. Chen, R. Ye, P. E. Cabrera, Y. Zhong, K. S. Wong, B. Z. Tang, *Chem. Commun.* **2012**, *48*, 10099–10101; c) L. Zhu, C. Y. Ang, X. Li, K. T. Nguyen, S. Y. Tan, H. Ågren, Y. Zhao, *Adv. Funct. Mater.* **2012**, *24*, 4020–4024; d) S. S. Palayangoda, X. Cai, R. M. Adhikari, D. C. Neckers, *Org. Lett.* **2008**, *10*, 281–284.
- [5] a) L. Wang, Y. Shen, M. Yang, X. Zhang, W. Xu, Q. Zhu, J. Wu, Y. Tian, H. Zhou, *Chem. Commun.* **2014**, *50*, 8723–8726; b) Y. Ren, F. Biegger, T. Baumgartner, *J. Phys. Chem. C* **2013**, *117*, 4748–4758; c) R.-H. Chien, C.-T. Lai, J.-L. Hong, *Macromol. Chem. Phys.* **2012**, *213*, 666–677; d) Z. Xie, C. Chen, S. Xu, J. Li, Y. Zhang, S. Liu, J. Xu, Z. Chi, *Angew. Chem. Int. Ed.* **2015**, *54*, 7181–7184; *Angew. Chem.* **2015**, *127*, 7287–7290; e) S. Shimizu, A. Murayama, T. Haruyama, T. Iino, S. Mori, H. Furuta, N. Kobayashi, *Chem. Eur. J.* **2015**, *21*, 1–9.
- [6] a) C. W. Liao, M. R. Rao, S. S. Sun, *Chem. Commun.* **2015**, *51*, 2656–2659; b) P. Galer, R. C. Korošec, M. Vidmar, B. Šket, *J. Am. Chem. Soc.* **2014**, *136*, 7383–7394; c) D. Ding, C. C. Goh, G. Feng, Z. Zhao, J. Liu, R. Liu, N. Tomczak, J. Geng, B. Z. Tang, L. G. Ng, B. Liu, *Adv. Mater.* **2013**, *25*, 6083–6088; d) L. Wang, W. Li, J. Lu, Y. X. Zhao, G. Fan, J. P. Zhang, H. Wang, *J. Phys. Chem. C* **2013**, *117*, 26811–26820; e) T. He, X. T. Tao, J. X. Yang, D. Guo, H. B. Xia, J. Jia, M. H. Jiang, *Chem. Commun.* **2011**, *47*, 2907–2909.
- [7] R. S. Singh, R. K. Gupta, R. P. Paitandi, M. Dubey, G. Sharma, B. Koch, D. S. Pandey, *Chem. Commun.* **2015**, *51*, 9125–9128.
- [8] a) B. Chen, X. Sun, R. E. Evans, R. Zhou, J. N. Demas, C. O. Trindle, G. Zhang, *J. Phys. Chem. A* **2015**, *119*, 8854–8859; b) C. Shi, Z. Guo, Y. Yan, S. Zhu, Y. Xie, Y. S. Zhao, W. Zhu, H. Tian, *ACS Appl. Mater. Interfaces* **2013**, *5*, 192–198; c) W. Z. Yuan, Y. Gong, S. Chen, X. Y. Shen, J. W. Y. Lam, P. Lu, Y. Lu, Z. Wang, R. Hu, N. Xie, H. S. Kwok, Y. Zhang, J. Z. Sun, B. Z. Tang, *Chem. Mater.* **2012**, *24*, 1518–1528; d) M. S. Kwon, J. Gierschner, S.-J. Yoon, S. Y. Park, *Adv. Mater.* **2012**, *24*, 5487–5492; e) B. Wang, Y. Wang, J. Hua, Y. Jiang, J. Huang, S. Qian, H. Tian, *Chem. Eur. J.* **2011**, *17*, 2647–2655.
- [9] a) W. Zheng, B.-B. Wang, C.-H. Li, J.-X. Zhang, C.-Z. Wan, J.-H. Huang, J. Liu, Z. Shen, X.-Z. You, *Angew. Chem. Int. Ed.* **2015**, *54*, 9070–9074; b) R. Fitzner, E. M. Osteritz, K. Walzer, M. Pfeiffer, P. Bäuerle, *Adv. Funct. Mater.* **2015**, *25*, 1845–1856; c) R. Stalder, D. Xie, A. Islam, L. Han, J. R. Reynolds, K. S. Schanze, *ACS Appl. Mater. Interfaces* **2014**, *6*, 8715–8722; d) Z.-F. An, C. Zheng, R.-F. Chen, J. Yin, J.-J. Xiao, H.-F. Shi, Y. Tao, Y. Qian, W. Huang, *Chem. Eur. J.* **2012**, *18*, 15655–15661; e) Y. Hong, J.-Y. Liao, D. Cao, X. Zang, D.-B. Kuang, L. Wang, H. Meier, C.-Y. Su, *J. Org. Chem.* **2011**, *76*, 8015–8021.
- [10] a) J. Min, Y. N. Luponosov, N. Gasparini, M. Richter, A. V. Bakirov, M. A. Shcherbina, S. N. Chvalun, L. Grodd, S. Grigorian, T. Ameri, S. A. Ponomarenko, C. J. Brabec, *Adv. Energy Mater.* **2015**, DOI: 10.1002/aenm.201500386; b) A. Baheti, K. R. J. Thomas, C.-P. Lee, C. T. Lib, K.-C. Ho, *J. Mater. Chem. A* **2014**, *2*, 5766–5779; c) S. Haid, A. Mishra, M. Weil, C. Urich, M. Pfeiffer, P. Bäuerle, *Adv. Funct. Mater.* **2012**, *22*, 4322–4333; d) J. Zhang, D. Deng, C. He, Y. He, M. Zhang, Z. G. Zhang, Z. Zhang, Y. Li, *Chem. Mater.* **2011**, *23*, 817–822.
- [11] a) S. Xu, Y. Yuan, X. Cai, C.-J. Zhang, F. Hu, J. Liang, G. Zhang, D. Zhang, B. Liu, *Chem. Sci.* **2015**, *6*, 5824–5830; b) Y. Zhang, D. Li, Y. Lia, J. Yu, *Chem. Sci.* **2014**, *5*, 2710–2716; c) X. Gu, J. Yao, G. Zhang, C. Zhang, Y. Yan, Y. Zhao, D. Zhang, *Chem. Asian J.* **2013**, *8*, 2362–2369; d) N. Zhao, C. Zhang, J. W. Y. Lam, Y. S. Zhao, B. Z. Tang, *Asian J. Org. Chem.* **2014**, *3*, 118–121.
- [12] W. Z. Yuan, F. Mahtab, Y. Gong, Z. Q. Yu, P. Lu, Y. Tang, J. W. Y. Lam, C. Zhu, B. Z. Tang, *J. Mater. Chem.* **2012**, *22*, 10472–10479.
- [13] M. Hepperle, J. Eckert, D. Gala, *Tetrahedron Lett.* **1999**, *40*, 5655–5659.
- [14] J. S. A. Brunskill, A. De, G. M. F. Vas, *Synth. Commun.* **1978**, *8*, 1–7.
- [15] Y. Yang, L. Zhang, C. Gao, L. Xu, S. Baia, X. Liu, *RSC Adv.* **2014**, *4*, 38119–38123.
- [16] a) H. Wang, G. Liu, H. Gao, Y. Wang, *Polym. Chem.* **2015**, *6*, 4715–4718; b) Q. Zhu, L. Huang, Z. Chen, S. Zheng, L. Lv, Z. Zhu, D. Cao, H. Jiang, S. Liu, *Chem. Eur. J.* **2013**, *19*, 1268–1280; c) R. Hu, E. Lager, A. A. Aguilar, J. Liu, J. Lam, H. Sung, I. Williams, Y. Zhong, K. Wong, E. P. -Cabrera, B. Z. Tang, *J. Phys. Chem. C* **2009**, *113*, 15845–15853.
- [17] a) J. Li, Y. Zhang, J. Mei, J. W. Y. Lam, J. Hao, B. Z. Tang, *Chem. Eur. J.* **2015**, *21*, 907–914; b) H. Li, Y. Guo, G. Li, H. Xiao, Y. Lei, X. Huang, J. Chen, H. Wu, J. Ding, Y. Cheng, *J. Phys. Chem. C* **2015**, *119*, 6737–6748.
- [18] Y. Zhang, J. Sun, G. Bian, Y. Chen, M. Ouyang, B. Hu, C. Zhang, *Photochem. Photobiol. Sci.* **2012**, *11*, 1414–1421.
- [19] N. Zhao, Z. Yang, J. W. Y. Lam, H. H. Y. Sung, N. Xie, S. Chen, H. Su, M. Gao, I. D. Williams, K. S. Wong, B. Z. Tang, *Chem. Commun.* **2012**, *48*, 8637–8639.
- [20] H. Li, J. Cheng, H. Deng, E. Zhao, B. Shen, J. W. Y. Lam, K. S. Wong, H. Wu, B. S. Li, B. Z. Tang, *J. Mater. Chem. C* **2015**, *3*, 2399–2404.
- [21] A. Mishra, R. K. Behera, P. K. Behera, B. K. Mishra, G. B. Behera, *Chem. Rev.* **2000**, *100*, 1973–2012.
- [22] R. Thomas, S. Varghese, G. U. Kulkarni, *J. Mater. Chem.* **2009**, *19*, 4401–4406.
- [23] D. D. Perrin, W. L. F. Armango, D. R. Perrin, *Purification of laboratory Chemicals*, Pergamon, Oxford, **1986**.
- [24] G. M. Sheldrick, *SHELXL97*, University of Göttingen, Göttingen, **1997**.
- [25] a) A. L. Spek, *PLATON*, Utrecht University, Utrecht, **2000**; b) A. L. Spek, *Acta Crystallogr. Sect. A* **1990**, *46*, 31.
- [26] Gaussian 09, Revision A.01, M. J. Frisch, G. W. Trucks, H. B. Schlegel, G. E. Scuseria, M. A. Robb, J. R. Cheeseman, G. Scalmani, V. Barone, B. Menonucci, G. A. Petersson, H. Nakatsuji, M. Caricato, X. Li, H. P. Hratchian, A. F. Izmaylov, J. Bloino, G. Zheng, J. L. Sonnenberg, M. Hada, M. Ehara, K. Toyota, R. Fukuda, J. Hasegawa, M. Ishida, T. Nakajima, Y. Honda, O. Kitao, H. Nakai, T. Vreven, J. A. Montgomery, Jr., J. E. Peralta, F. Ogliaro, M. Bearpark, J. J. Heyd, E. Brothers, K. N. Kudin, V. N. Staroverov, R. Kobayashi, J. Normand, K. Raghavachari, A. Rendell, J. C. Burant, S. S. Iyengar, J. Tomasi, M. Cossi, N. Rega, J. M. Millam, M. Klene, J. E. Knox, J. B. Cross, V. Bakken, C. Adamo, J. Jaramillo, R. Gomperts, R. E. Stratmann, O. Yazyev, A. J. Austin, R. Cammi, C. Pomelli, J. W. Ochterski, R. L. Martin, K. Morokuma, V. G. Zakrzewski, G. A. Voth, P. Salvador, J. J. Dannenberg, S. Dapprich, A. D. Daniels, Ö. Farkas, J. B. Foresman, J. V. Ortiz, J. Ciołowski, D. J. Fox, Gaussian, Inc. Wallingford CT, **2009**.

Received: September 7, 2015

Published online on November 30, 2015